DARK ENERGY FROM THE LOG-TRANSFORMED CONVERGENCE FIELD

HEE-JONG SEO[1], MASANORI SATO[2], MASAHIRO TAKADA[3], AND SCOTT DODELSON[4,5]
Draft version September 27, 2011

ABSTRACT

A logarithmic transform of the convergence field improves 'the information content', *i.e.*, the overall precision associated with the measurement of the amplitude of the convergence power spectrum by improving the covariance matrix properties. The translation of this improvement in the information content to that in cosmological parameters, such as those associated with dark energy, requires knowing the sensitivity of the log-transformed field to those cosmological parameters. In this paper we use N-body simulations with ray tracing to generate convergence fields at multiple source redshifts as a function of cosmology. The gain in information associated with the log-transformed field does lead to tighter constraints on dark energy parameters, but only if shape noise is neglected. The presence of shape noise quickly diminishes the advantage of the log mapping, more quickly than we would expect based on the information content. With or without shape noise, using a larger pixel size allows for a more efficient log-transformation.

Subject headings: cosmology: theory - gravitational lensing large-scale structure methods: numerical

1. INTRODUCTION

The nature of the dark energy is one of the most intriguing mysteries of the Universe. As a result, various large sky area surveys are being conducted and designed to statistically determine the properties of this energy component with high precision. We of course wish to extract the most information available from the data. Recently, it has been suggested that the two-point statistics of the logarithmically transformed nonlinear density or weak-lensing convergence field may contain more information than the conventional nonlinear fields without the transformation (e.g., Neyrinck et al. 2009; Seo et al. 2011). In linear theory (i.e., at high redshift), the convergence (and density) field is Gaussian, which means that the two-point function contains all the information. Due to the structure growth, the field however becomes more nonlinear and non-Gaussian at low redshift. The cosmological information in the two-point function therefore decreases with increasing nonlinearity, the lost information moving to the higher order statistics (Takada & Jain 2004).

A logarithmic transform of the nonlinear mass/galaxy density field or the weak-lensing convergence field, which makes the one-point distribution of the field more Gaussian (e.g., Coles & Jones 1991; Kayo et al. 2001; Taruya et al. 2002), appears to produce a final field that alleviates this problem by mimicking properties of a Gaussian field (Neyrinck et al. 2009; Seo et al. 2011; Yu et al. 2011). The two-point function of the transformed field has a more diagonal covariance matrix (e.g., Neyrinck et al. 2011a) and (therefore) increased information content (*i.e.*, the overall precision associated with the measurement of the amplitude of the convergence/density power spectrum) to a level comparable to the Gaussian field.

[1] Berkeley Center for Cosmological Physics, LBL and Department of Physics, University of California, Berkeley, CA, USA 94720. hee-jongseo@lbl.gov

[2] Department of Physics, Nagoya University, Nagoya 464-8602, Japan

[3] Institute for the Physics and Mathematics of the Universe (IPMU), University of Tokyo, Chiba 277-8582, Japan

[4] Center for Particle Astrophysics, Fermi National Accelerator Laboratory, Batavia, IL 60510

[5] Department of Astronomy & Astrophysics, The University of Chicago, Chicago, IL 60637

Seo et al. (2011) showed that a Taylor expansion of the logarithmic transformation that includes up to the bispectrum contribution captures most of the improvement on large scales, suggesting that the log-transform draws its extra information from higher order statistics.

In these works, the benefits of the log-transform have been studied only when a single parameter – the amplitude of the power spectrum – is varied. This does not necessarily translate into an improvement in the measurements of other cosmological parameters, such as dark energy parameters. If the power spectrum of the transformed field is less sensitive to, *e.g.*, dark energy (*i.e.*, smaller derivatives with respect to the parameters), or suffers more degeneracies between parameters, the log-transform may not be as effective as expected based on the improved information content. In order to test this, we need to understand the dependence of the log-transformed field as a function of cosmology. In Seo et al. (2011), which we refer to as Paper I hereafter, we used a modified log-transform for the weak-lensing convergence field and showed the increased information content after the log transform. Here we extend the previous work and investigate whether or not this improvement propagates to the determination of the dark energy parameters. A first step in this direction was taken in Joachimi et al. (2011) for the weak lensing field, wherein mapping the required derivatives with respect to cosmological parameters were computed analytically. They showed that the Box-Cox transformation that encloses the logarithmic transformation, when optimized, indeed gives a tighter constraint on $\Omega_m - \sigma_8$. Also, Neyrinck (2011c) has recently shown that, using Coyote Universe simulations (Heitmann et al. 2010), log-transformed density field gives tighter, but unmarginalized, constraints on cosmological parameters.

Here, we adopt a more extensive numerical approach and derive the dependence of the transformed field on the cosmological parameters directly from a very large set of N-body simulations produced for various cosmologies. The total simulated sky is 37000 square degrees. We produce mock weak-lensing convergence fields at three source redshifts, carry out a Fisher matrix analysis of tomography using the fully non-linear covariance matrix and derivatives, and derive marginal-

ized errors on 6-8 cosmological parameters, including dark energy parameters (*i.e.*, Ω_X, w_0, and w_a). As far as we know, this paper is the first to conduct the full Fisher matrix analysis of weak-lensing power spectrum tomography using the numerical simulations to compute the derivatives and covariance matrices (but also see Yang et al. 2011, for peak statistics tomography).

The paper is organized as following. In § 2, we explain the details of our *N*-body simulations and Fisher matrix analysis. In § 3, we revisit the general properties of the log transform, such as the one-point probability distribution function (PDF), the information content, and the covariance matrix from the *N*-body results using three source redshift bins. In § 4, we present the numerical derivatives before and after the logarithmic mapping and the results of the full Fisher matrix analysis, deriving the dark energy figure-of-merit. We compare this result with the Fisher matrix obtained from semi-analytic fits to the power spectrum. In § 5, we include shape noise; in § 6, we discuss the effect of the size of pixels; in § 7, we discuss the analytic, Gaussian Fisher matrix results in comparison to our *N*-body results for the fiducial field. Finally, we conclude in § 8.

2. NUMERICAL FISHER MATRIX ANALYSIS

To study the cosmological information from the log-transformed field numerically, we use a large set of ray-tracing simulations. The ray-tracing simulations are constructed from 2×200 realizations of *N*-body simulations with box sizes of 240 and $480 h^{-1}$Mpc on a side, respectively. The number of particles in each simulation is 256^3. For the fiducial cosmology, we adopt the concordance ΛCDM model: matter fraction $\Omega_m = 0.238$, baryon fraction $\Omega_b = 0.042$, dark energy fraction $\Omega_X = 0.762$ (therefore a flat universe), the equation of state parameters $w_0 = -1$ and $w_a = 0$, spectral index $n_s = 0.958$, normalization $A_s = 2.35 \times 10^{-9}$, and Hubble parameter $h = 0.732$. Note that the fiducial cosmology gives $\sigma_8 = 0.76$ (the variance of the present-day density fluctuation in a sphere of radius $8 \, h^{-1}$Mpc). We assume three delta-function like source redshifts at $z = 0.6$, 1.0, and 1.5 for a tomographic study. From the 400 *N*-body simulations, we generate 1000 realizations of $5° \times 5°$ lensing convergence fields (i.e., a total of 25000 square degrees) with 2048^2 pixels (0.15 arcmin per pixel) at each source redshift using ray-tracing (a total of 3000 convergence fields). Details of the ray-tracing can be found in Sato et al. (2009) (see, also Sato et al. 2011).

We resample the convergence fields in 128^2 pixels (2.4 arcmin per pixel) by averaging over nearby 16 by 16 pixels as our fiducial case. As will be discussed in § 6, we find that using a larger pixel leads to a more efficient logarithmic mapping. We compute the power spectra of the 3×1000 convergence fields assuming periodic boundary conditions before and after logarithmic mapping. The covariance matrix is derived by calculating covariance between band powers at different wavenumber bins and at different source redshifts. The resulting covariance matrix represents dispersions in the lensing power spectra for an area of $5° \times 5°$. We assume a future, wide-field weak lensing survey of 5000 square degrees, just as in the Dark Energy Survey (DES; Abbott et al. 2005), by rescaling each elements of the covariance matrix by $1/(5000/25)$.

2.1. *l bin width*

For the power spectrum and the covariance calculations, we need to determine the multipole bin width. An important requirement is that the dimension of the covariance matrix is smaller than the total number of realizations that are used for generating it. The dimension of the covariance matrix with three source redshift bins is three times bigger than that with a single source redshift bin. We choose $\Delta l = 200$ so that going up to $l_{\max} = 2000$ requires a 30 by 30 covariance matrix. The dimension of the covariance matrix is then smaller than the 1000 realizations. Another reason for using $\Delta l = 200$ rather than a smaller bin width is to reduce the sample variance effect in the derivatives calculation and therefore to make the derivatives smoother.

2.2. *Log-mapping*

We use the logarithmic mapping that was introduced in Paper I. A log field is defined as:

$$\kappa_{\ln}(\vec{\theta}) \equiv \kappa_0 \ln \left[1 + \frac{\kappa(\vec{\theta})}{\kappa_0} \right], \qquad (1)$$

where κ_0 is a constant with a value slightly larger than the absolute value of the minimum value of κ for a given cosmology, source redshift, and survey pixel – this keeps the argument of the logarithm positive. In detail, to generate the covariance matrix for the fiducial cosmology, we use $\kappa_0 = |\kappa_{\min}| + 0.001$ where $\kappa_{\min}$ is the minimum pixel κ of the 1000 convergence fields at each source redshift: $\kappa_{\min} = -0.01348, -0.02940, -0.04874$ at source redshifts $z_s = 0.6$, 1, and 1.5, respectively. While $\kappa_{\ln}$ reduces to the standard convergence in the limit of small κ, the log alters κ in very high or low convergence regimes. The parameter κ_0 tunes the degree of the alteration such that, the smaller κ_0, the more we alter the field. Note that various properties of the $\kappa_{\ln}$ field that will be discussed in this paper show a slow, asymptotic behavior as a function of κ_0 near the minimum value of κ. Therefore fine-tuning is not necessary for κ_0.

2.3. *Derivatives*

For the Fisher matrix calculation, we need to first calculate numerical derivatives of the lensing power spectra with respect to cosmological parameters. To do this, we ran ray-tracing simulations of the convergence fields for cosmological models perturbed around the fiducial cosmology. We varied each of the following cosmological parameters: A_s, n_s, the cold dark matter density $\Omega_c h^2$ (the fiducial values for $\Omega_c h^2 = 0.1054$), Ω_X, and w_0 by $\pm 10\%$, respectively, and w_a by ± 0.5, respectively. The Hubble parameter h, Ω_m, and Ω_b[6] are then dependent parameters. For each of the 12 different cosmological models, we built 40 realizations of the convergence fields for each of the three redshift bins. Therefore we use a total of $3(40 \times 12) = 1440$ simulated convergence fields for calculating the derivatives. We then computed power spectra with and without the logarithmic transformation from each realization, averaged them, and derived the derivatives by differencing them. The value $\kappa_{\min}$ (Eq. 1) is derived for each cosmology and therefore different for different cosmological models. Meanwhile, calculating derivatives becomes tricky in the presence of shape noise for the logarithmic transformation, as will be discussed in the next section.

---

[6] We hold $\Omega_b h^2$ fixed.

2.4. *Shape noise*

The intrinsic ellipticities of source galaxy shapes cause white noise contamination to the lensing power spectrum (Kaiser 1998). For the simulated convergence map, we can include the noise contamination by adding, to each pixel, random Gaussian noise with variance

$$\sigma_N^2 = \frac{\sigma_\epsilon^2}{\bar{n}_g \Omega_{\rm pix}}, \tag{2}$$

where σ_ϵ is the rms of intrinsic shear per component, $\bar{n}_g$ is the mean number density of galaxies and $\Omega_{\rm pix}$ is the pixel area. We set $\sigma_\epsilon = 0.22$ and $\bar{n}_g = 30$ arcmin^{-2} as for our fiducial values at each redshift, therefore a total of 90 galaxies per arcmin^2, which is much deeper than current weak lensing surveys such as Dark Energy Survey (Abbott et al. 2005). In the presence of shape noise, the fiducial, κ, field is closer to a Gaussian field and $|\kappa_{\rm min}|$ becomes larger than without shape noise; the log-transform becomes less efficient. We measure $\kappa_{\rm min}$ in the presence of the shape noise and use it when calculating the covariance matrix of the log-transformed field.

For the fiducial field before log mapping, we calculate the derivatives from the power spectra without shape noise, because the shape noise does not depend on cosmological parameters. That is, the shape noise is included only in the covariance matrix. This is consistent with what we would do in the likelihood analysis with real data. We would derive a signal power spectrum after subtracting the shape noise contribution (Hikage et al. 2011) and compare it with a theory power spectrum as a function of cosmology.

Including the shape noise effect in the derivatives calculation is non-trivial for the log-transformed field. The shape noise not only increases noise in the measured convergence field, but also makes the log-transform less efficient by increasing $|\kappa_{\rm min}|$. That is, when a convergence field is optimally log-transformed by using $\kappa_{\rm min}$, the power spectrum is different for a different level of shape noise even after the shape noise is, ideally, subtracted. In addition, while we conduct a nominal subtraction of the shape noise from the power spectrum by subtracting a constant number that is derived from the difference in the variance of the field before and after the log-transform in the presence of shape noise, in truth, the effect of the shape noise is neither scale-independent nor cosmology-independent in the log-transformed field due to the nonlinear transformation. Therefore we need to derive the derivatives differently for different cosmologies for the log-transformed field. For each of the 12 cosmological model, we first estimated the $\kappa_{\rm min}$ value for the log-transformed field with the shape noise. In order to minimize the impact of the random noise on the derivative calculation, for each cosmology, we cloned each of the 40 realizations 25 times using a different random seed for the shape noise. This way we generate 1000 realizations from the underlying 40 realizations for each cosmology; the averaged power spectrum will have much smaller sample variance on the effect of shape noise. We then log-transform the fields and differentiate the resulting power spectra between different cosmologies and calculated the derivatives with respect to cosmological parameters.

2.5. *Fisher matrix*

We want to propagate the errors on the convergence power spectrum, our observable, into the projections of cosmological parameters using a Fisher information matrix formalism. Using the numerical nonlinear derivatives and the measured covariance matrices, we can compute the Fisher information matrix for cosmological parameters of our interest, p_i, (Tegmark 1997; Tegmark et al. 1997):

$$F_{ij}^{\rm WL} \equiv \sum_{z_s, z_s'} \sum_{l, l' < l_{\rm max}} \frac{\partial C_{z_s}(l)}{\partial p_i} {\rm Cov}^{-1}(l, z_s, l', z_s') \frac{\partial C_{z_s'}(l')}{\partial p_j}, \tag{3}$$

where $C_{z_s}(l)$ is the measured convergence power spectrum at multipole bin l and z_s; Cov is the measured covariance matrix between wavenumbers and source redshifts. The set of cosmological parameters is: the amplitude of the power spectrum ($\ln A_S$), the slope of the primordial spectrum (n_s), the physical matter density in units of the critical density ($\Omega_m h^2$), the dark energy density Ω_X, and two parameters for the dark energy equation of state: $w = w_0 + z/(1+z)w_a$. Note that, by incorporating the information from the three source redshifts into the Fisher matrix, we are including the tomographic lensing information (Hu 1999; Takada & Jain 2004). The error on the i-th parameter including marginalization over uncertainties in other parameters is estimated as $\sigma(p_i) = \sqrt{(\boldsymbol{F}^{-1})_{ii}}$, where $\boldsymbol{F}^{-1}$ is the inverse of the Fisher matrix. The unmarginalized error is given as $\sigma(p_i) = 1/\sqrt{F_{ii}}$. We have also tried including independent, free shape noise as parameters for the three redshift bins, but find little effect on the constraints we derive.

2.6. *Planck prior*

Lensing information alone cannot determine all the cosmological parameters simultaneously due to severe parameter degeneracies. We therefore include in these projections the CMB information expected from the Planck experiment. The CMB is sensitive to two additional parameters, the baryon density $\Omega_b h^2$ and curvature density Ω_K. We combine the convergence field information with the Planck prior (Hu 2002) by adding the 8×8 Planck Fisher matrix to the 6×6 dimensional convergence Fisher matrix:

$$F_{ij} = F_{ij}^{\rm WL} + F_{ij}^{\rm cmb}, \tag{4}$$

where the lensing Fisher matrix $F_{ij}^{\rm WL}$ has non-zero entries in the 6×6 block associated with $\ln As$, n_s, $\Omega_c h^2$ (or $\Omega_m h^2$), Ω_X, w_0, and w_a, and the Planck Fisher matrix $F_{ij}^{\rm cmb}$ has non-zero entries in all 8×8 elements including additional two parameters: $\Omega_b h^2$ and Ω_K. The Planck Fisher matrix we use includes marginalization over uncertainties in the optical depth parameter τ on which the CMB power spectra depend. The zero Ω_K and $\Omega_b h^2$ elements in the convergence Fisher matrix reflect the fact that these two parameters are constrained solely by the CMB information.

3. GENERAL PROPERTIES OF THE LOG TRANSFORMATION

Before presenting the Fisher matrix analysis, we first revisit the general properties of the log-transform that have been discussed in Paper I, such as the power spectra, 1-point probability distribution (PDF), the information content, and the structure of the covariance matrix for the three source redshift bins.

The upper left panel of Figure 1 shows the measured power spectra of the convergence field κ (open symbols and/or dashed lines) and the log-transformed field $\kappa_{\rm ln}$ (solid symbols and/or solid lines) at $z_s = 0.6$ (triangles and/or black),
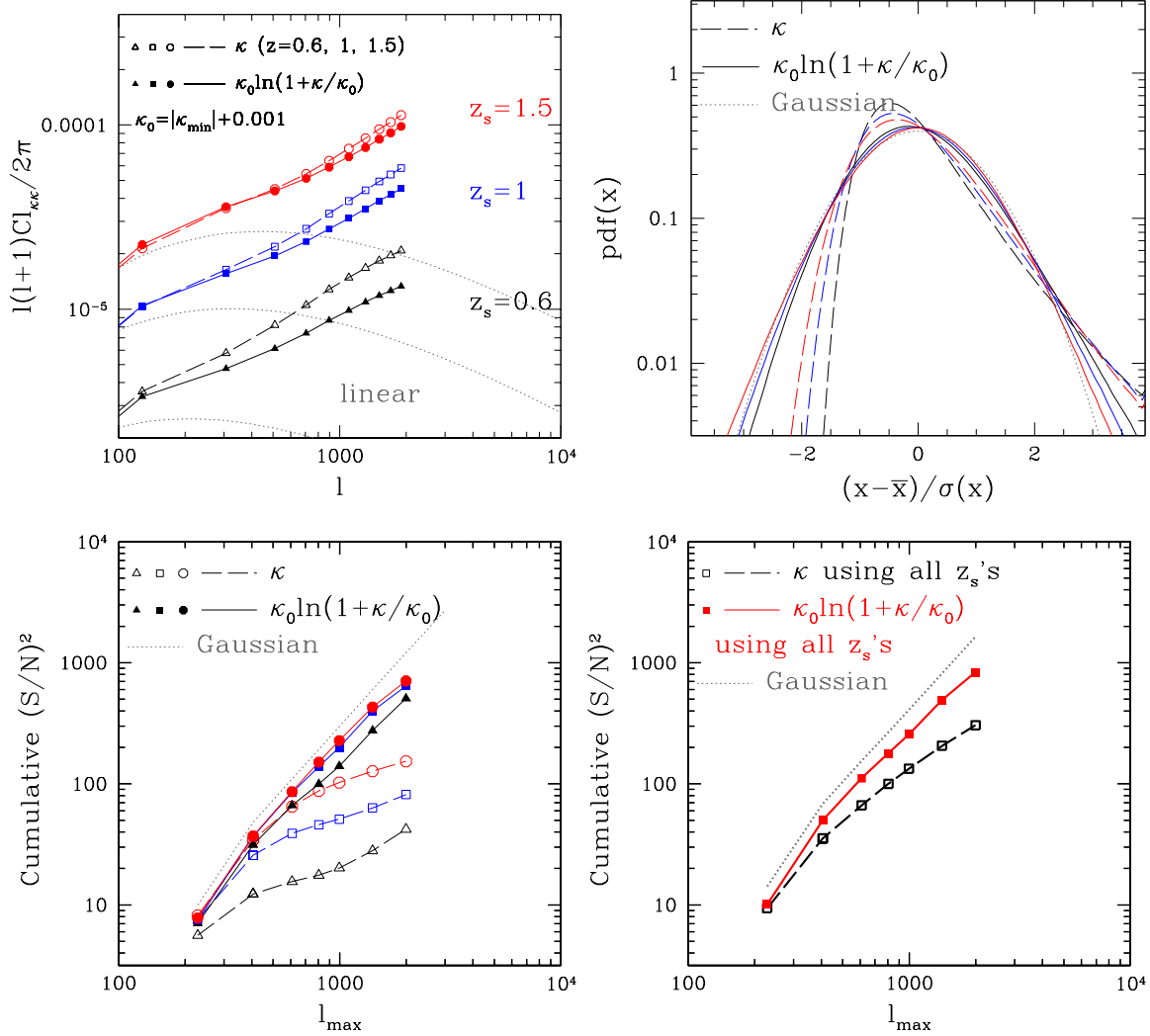
FIG. 1.— Upper left: power spectra at $z = 0.6$ (black), 1 (blue), and 1.5 (red) before (dashed lines/open points) and after the log-transform (solid lines/filled points). Upper right: PDF distribution before and after the log-transform. Lower left: the information content of the individual redshift bins. Lower Right: the information content from the combination of the three z_s bins. Since the three bins share information, the combination of the three bins (solid and dashed lines with points) show less improvement after the logarithmic transformation. Dotted lines show the Gaussian limit.

1 (squares and/or blue), and 1.5 (circles and/or red). As expected, the log-transform reduces the small-scale nonlinear clustering. The reduction is more prominent for the lower source redshift, the reason for which is apparent in the PDF distribution in the upper right panel: the PDF of κ deviates more from a Gaussian PDF at $z_s = 0.6$ and therefore is more improved by the log-mapping. The lower left panel shows the improvement in the information content, the cumulative signal-to-noise ratio $(S/N)^2$ integrated up to a given maximum multipole l_{max}, for each of the three z_s bins, defined as:

$$\left[\frac{S}{N}(l_{max})\right]^2 \equiv \left[\sum_{l,l'<l_{max}} C_l \text{Cov}^{-1}(l,l') C_{l'}\right] \quad (5)$$

where C_l is the power spectrum of multipole l before and after the log-transform, Cov is the covariance matrix describing correlations between the power spectra of multipoles l and l' ($l, l' < l_{max}$) at each z_s, and the summation runs over all the multipoles l and l' subject to $l, l' < l_{max}$ (Sato et al. 2009; Takahashi et al. 2009). As pointed out in Paper I, this information content can be understood as the inverse of the fractional error on the amplitude of the observed, nonlinear power spectrum before and after the logarithmic transform. The Fisher matrix analysis will show to what extent this improved fractional error on the observed amplitude remains when a full set of cosmological parameters is used. In the lower left panel, the improvement in the information content due to the log-transform is largest for $z_s = 0.6$ and smallest for $z_s = 1.5$ due to the level of nonlinearities, as expected from the upper two panels. The dotted gray line is the $(S/N)^2$ expected for a Gaussian case. Due to the nonlinear structure growth that causes significant off-diagonal covariances, the measured $(S/N)^2$ values of the κ field are much smaller than the Gaussian limit. We find that the κ_{ln} field returns the $(S/N)^2$ closer to that of the Gaussian case, which confirms the results in Paper I but using a different Δl. The improvement is a factor of $\sim$ 6.9, 3.9, and 2.2 at $z_s = 0.6$, 1, and 1.5, respectively, at $l_{max} \sim 1000$ and a factor of 12, 7.9, 4.6, respectively at
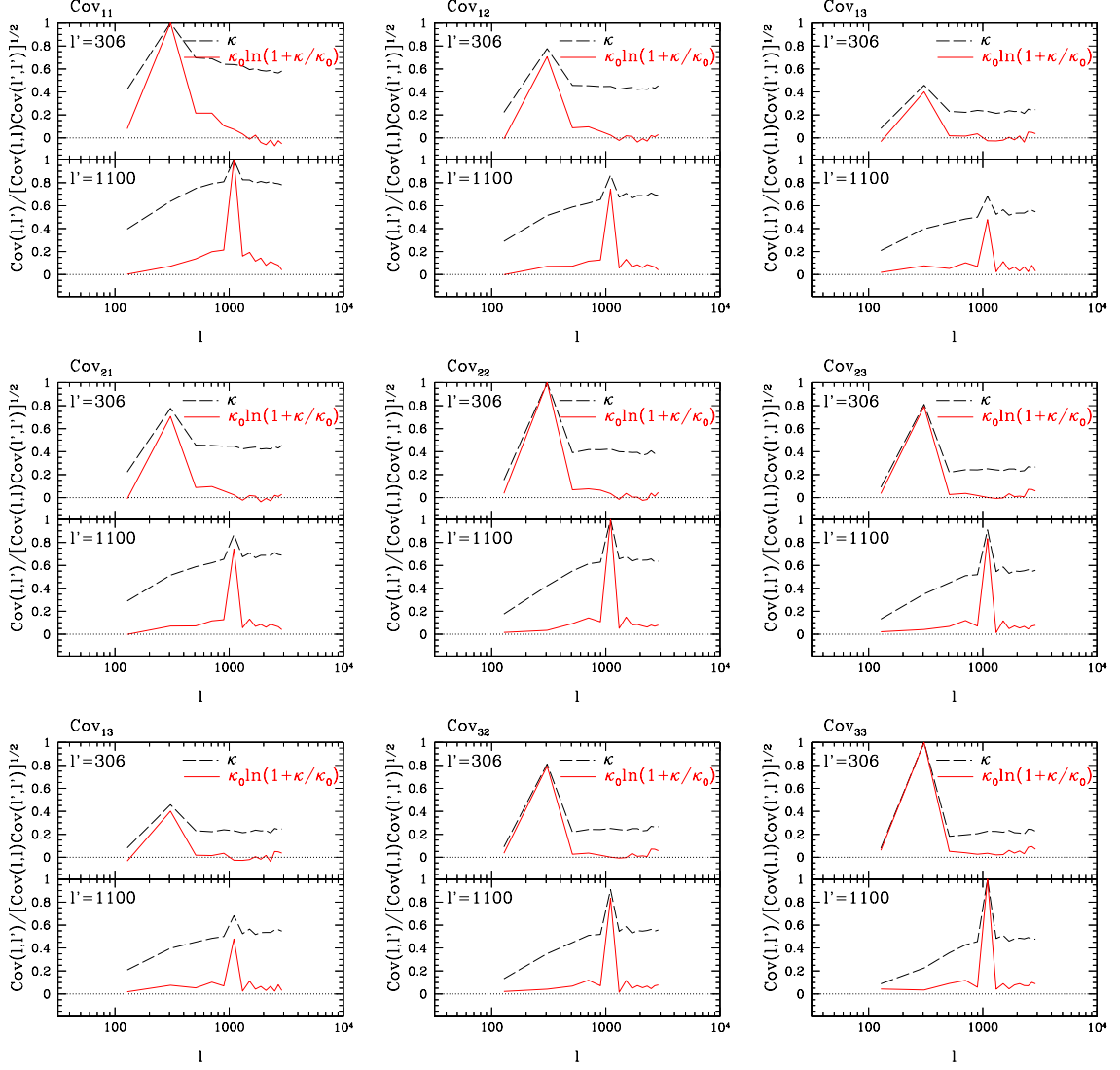
FIG. 2.— Slices of the covariance matrix to show the covariance matrix property before (black dashed) and after (red solid) the log transform. Each panel shows a different block of the covariance matrix constructed by pairing two of the three z_s bins. The elements are normalized relative to the diagonal elements, i.e., $\mathrm{Cov}(l, l')/(\mathrm{Cov}(l, l)\mathrm{Cov}(l', l'))^{1/2}$. In the notation Cov_{ij}, i and j indicates a source redshift bin. For example, Cov_{11} is the normalized auto covariance matrix of $z_s = 0.6$. For each block of the covariance matrix, we find that the κ_{ln} field is much more diagonal than κ. That is, the covariance between different l bins is significantly reduced after the log-transform, while the covariance between different z_s given l remains similar before and after the log-transform.

$l_{\max} \sim 2000$; note that the improvement is largest for the lowest source redshift. The improvement is slightly better than was reported in Paper I, which is mainly due to the logarithmic transformation seemingly being more efficient for the larger pixels used here. The lower right panel shows the improvement in the information content when the information from the three z_s bins is combined. This is done by including the measured covariance between different z_s bins in Cov in Eq. (5) and summing the signal-to-noise ratios up to $l_{\max}$ and over all the three z_s bins. Since the three z_s bins share some of the lensing structures, there are non-vanishing covariances between the power spectra of different z_s bins and therefore the improvement due to the log-transform is somewhat smaller when all z_s are combined: 1.9 at $l_{\max} = 1000$ and 2.7 at $l_{\max} = 2000$. The Gaussian case in the lower right panel is derived also taking into account the expected covariance between different redshift bins.

In addition to the improved information content, one of the potentially advantageous features of the log-mapping is the improvement in the covariance matrix property: it reduces the size of the off-diagonal terms (Paper I). Figure 2 shows two rows of the covariance matrix for $l = 306$ and $l = 1100$. Each panel shows a different block of the normalized covariance matrix constructed by pairing two of the three z_s bins. For each block of the covariance matrix, we find that the κ_{ln} field is much more diagonal than κ. That is, the covariance between different l bins is significantly reduced by the log-transform. Both κ and κ_{ln} fields show a slightly higher level of off-diagonal covariance compared to what we found in Paper I, partly due to the larger Δl bin used here (i.e., $\Delta l = 200$ compared to $\Delta l = 100$ in Paper I) and also probably due to sample variance. Note that the different bin width alters only the Gaussian covariance contribution (Meiksin & White 1999; Scoccimarro et al.
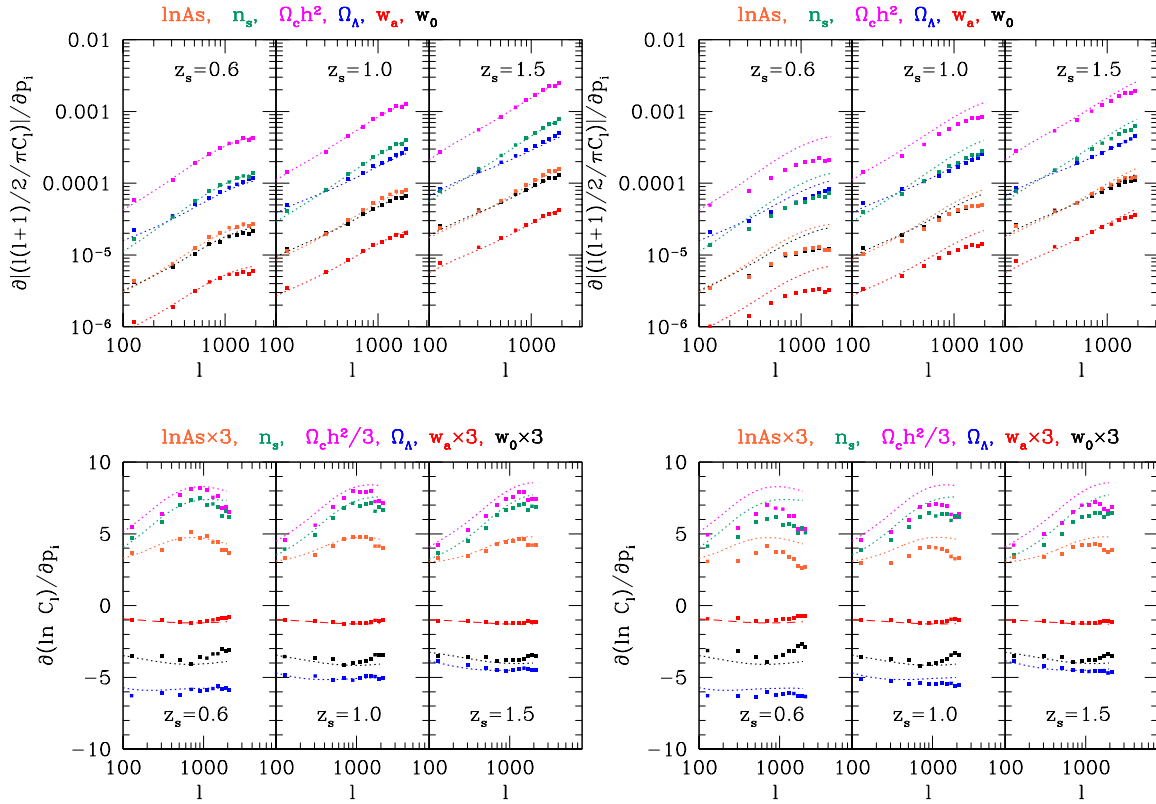
FIG. 3.— Derivatives of convergence power spectra of κ and $\kappa_{\ln}$ fields with respect to various cosmological parameters in absolute values. Points are derivatives estimated from N-body simulations; dotted lines use Halofit (for the fiducial map) as a comparison. Left: the fiducial map. Right: the log-mapping. The fractional derivatives (bottom panels) remain similar even after the log-transform for some parameters, especially at high source redshifts. The fractional derivatives are rescaled by the factor denoted in the legends for clarity.

1999; Cooray & Hu 2001; Takada & Jain 2009); the larger bin width reduces the Gaussian covariance, the diagonal components of the covariance matrix, and thus increases the relative off-diagonal components. While the covariance between different wavenumbers is decreased, the covariance between different z_s given l remains similar before and after the log-transform by looking at the location of the peaks in Cov_{ij} for $i \neq j$.

In summary, we observe general properties of the log-transform that are consistent with the results in Paper I: the 1-point PDF is more Gaussian, the covariance matrix is closer to a diagonal matrix, and the information content is greatly improved after the log-transform. We next propagate this improvement to the errors on cosmological parameters using the Fisher matrix formalism.

4. FISHER MATRIX ANALYSIS

We study how the improvement on the precision of the amplitude, or the information content, propagates into the precision of cosmological parameters. The improvement in the information content for the $\kappa_{\ln}$ field is due to the improved properties of its covariance matrix. The Fisher matrix formalism then combines this with an extra piece: the sensitivity of the κ and $\kappa_{\ln}$ power spectra to cosmological parameters.

Before presenting the Fisher matrix results, we take a look at the numerical derivatives calculated from the convergence fields from a large set of N-body simulations. Figure 3 shows the derivatives of the power spectrum of κ (left panels) and

$\kappa_{\ln}$ (right panels) fields with respect to various cosmological parameters (square points). As a comparison, the dotted lines show the prediction based on Halofit (Smith et al. 2003) for the fiducial mapping. We see an obvious decrease in the relative amplitude of the derivatives due to the log-transform (bottom panels) at $z_s = 0.6$. Such changes in the derivatives will be combined with the changes in the covariance matrix property in the Fisher matrix calculation. As a caveat, we find the relative amplitude of the derivative with respect to n_s decreases after the log-transform, while Neyrinck (2011c) finds an increase on small scales; it might be due to a difference in details of the log-transform between the weak lensing field and the density field.

4.1. Without Planck prior

We first show the Fisher matrix results of the convergence field without shape noise contamination and CMB information in Figure 4. We use all the information up to $l = 2000$. For reference, if the amplitude of the power spectrum were the only parameter (as in Paper I), the log field would lead to an error $\Delta \ln(A_s) = 1.9 \times 10^{-3}$ for these survey parameters while the standard κ field would have $\Delta \ln(A_s) = 2.9 \times 10^{-3}$. We call this a factor of 1.5 improvement in the *1D Figure of Merit*. When we generalize to 6 parameters, the corresponding Figure of Merit (FoM, hereafter) is the square root of the determinant of the 6×6 Fisher matrix. In this case, we find a factor of 23 improvement. This is better than the naive expectation of $1.5^6 = 11$, so our first conclusion is that the advan-

TABLE 1
MARGINALIZED ERRORS ON EACH PARAMETERS.

	$\ln A_s$	n_s	$\Omega_m h^2$	Ω_X	w_0	w_a	$\Omega_b h^2$	Ω_K
κ alone	0.0642	0.897E-02	0.493E-02	0.472E-02	0.458E-01	0.119		
$\kappa_{\ln}$ alone	0.0408	0.674E-02	0.325E-02	0.202E-02	0.189E-01	0.124		
κ + Planck	0.0101	0.336E-02	0.115E-02	0.367E-02	0.357E-01	0.997E-01	0.150E-03	0.272E-02
$\kappa_{\ln}$ + Planck	0.0102	0.304E-02	0.107E-02	0.149E-02	0.161E-01	0.632E-01	0.148E-03	0.253E-02

NOTE. — Marginalized errors before and after the log-transform using power spectrum information up to $l_{\max} = 2000$. Both errors show distinct improvement after log-transform; the improvement is mainly on Ω_X, w_0 and w_a once the Planck prior is included.
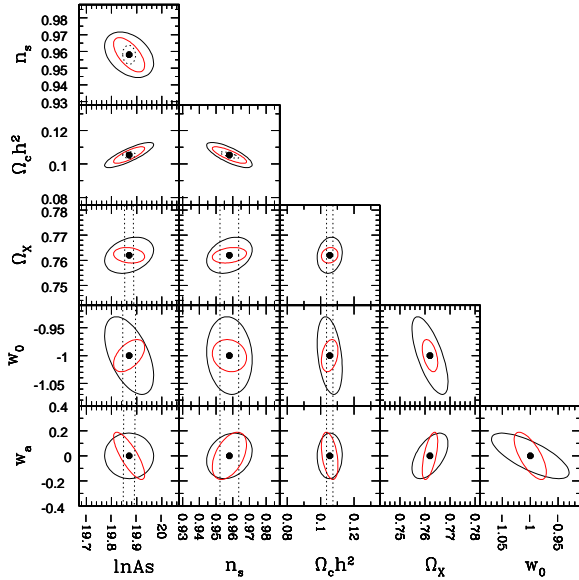

FIG. 4.— Marginalized error contours before (solid black lines) and after log-transform (red lines) without shape noise contamination and CMB information. That is, we took the 2×2 sub-Covariance matrix and plotted the error contours. We use power spectrum information up to $l = 2000$. One sees that the marginalized errors are overall smaller for $\kappa_{\ln}$. The dotted contours show constraints from the Plank alone. The Planck contours for pairs between Ω_X, w_0, and w_a do not show up here due to the extreme degeneracies.
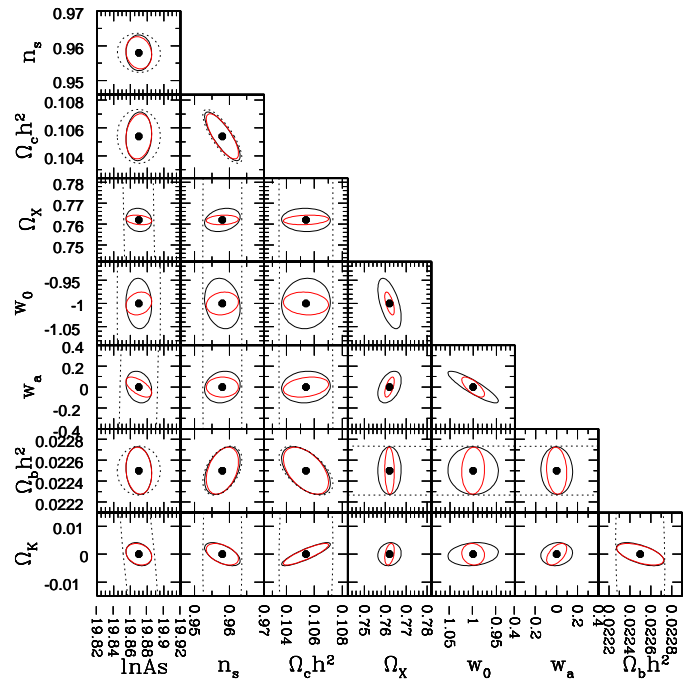

FIG. 5.— Marginalized error contours before (solid black lines) and after log-transform (red lines) when we combine the weak lensing data with the Planck mission. We use power spectrum information up to $l = 2000$. One sees that $\kappa_{\ln}$ improves constraints mainly on the three dark energy parameters, i.e., Ω_X, w_0, and w_a.

tages of the log estimator hold up – or even increase – when generalizing to multiple cosmological parameters.

Figure 4 shows some 2D slices of these constraints. The figure shows the marginalized $1 - \sigma$ error contours from weak lensing tomography alone for various pairs of the 6 cosmological parameters[7]. The solid black lines show the result from the κ field before the log mapping and the red lines show the results of the $\kappa_{\ln}$ field. The constraints are tighter for the $\kappa_{\ln}$ field: the error ellipses have shrunk and the projections are that the $\kappa_{\ln}$ field often leads to narrower allowed regions. Table 1 lists the marginalized errors without the Planck prior: the log-transform shows improvement, especially on Ω_X and w_0. The dotted contours in Figure 4 show constraints from Planck alone: the Planck contours for pairs between Ω_X, w_0, and w_a do not show up here due to the extreme degeneracies. For all parameters other than the dark energy parameters, the information from the Planck mission dominates.

4.2. With Planck prior

The situation is qualitatively similar when the Planck prior is added in. The Figure of Merit (now 8D) is larger by a factor of 12 when the log estimator is used. Figure 5 shows slices

[7] I.e., we take the 2×2 sub-Covariance matrix and plot the error contours.

of the error contours on the 8 cosmological parameters when we combine the weak lensing data with Planck (left panel). The solid black line is for the κ field and the red line for the $\kappa_{\ln}$ field after the Planck Fisher matrix is combined. The dotted contour shows the error contours for the Planck alone as a comparison. When the Planck priors are included, the information on parameters other than Ω_X, w_0, and w_a is dominated by the Planck information, as evident in Figure 4; $\kappa_{\ln}$ improves constraints mainly on the three dark energy parameters [8]. Table 1 shows that we achieve an improvement by a factor of 2.5 for Ω_X, 2.2 for w_0, and 1.6 for w_a by log-transformation.

4.3. Improvement in the dark energy FoM

[8] The solid contours in Figure 5 do not exactly agree with the naive error contour combination of the solid contours in Figure 4 and the dotted Planck contour: we would expect this agreement if we add the Fisher matrices from the 2 by 2 sub-covariance matrices of the convergence field and the Planck mission. However we are adding the two full Fisher matrices here such that a given marginalized error contour is affected by the effect of the Planck information on the rest of the parameters.
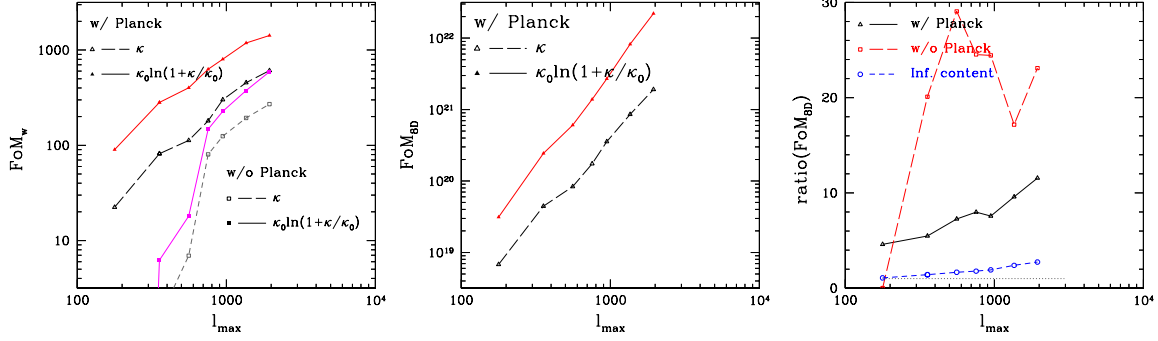
FIG. 6.— Figure of Merit in w_0-w_a (Left) and in the 8-D (middle) before and after the log-transform. The magenta and gray lines with squares in the left panel show the result without the Planck prior while the red and black triangles show the values with the Planck prior. We find more than a factor of 2 improvement in $\mathrm{FoM}_{w_0-w_a}$. The middle panel shows a 8-dimensional figure-of-merit, i.e., the inverse volume of the 8-dimensional parameter space. The right panel shows the ratio of the 8-D FoM between with and without the log-transform. We find a factor of 7-12 improvement using $l_{\max} = 1000 - 2000$ in the presence of the Planck prior.
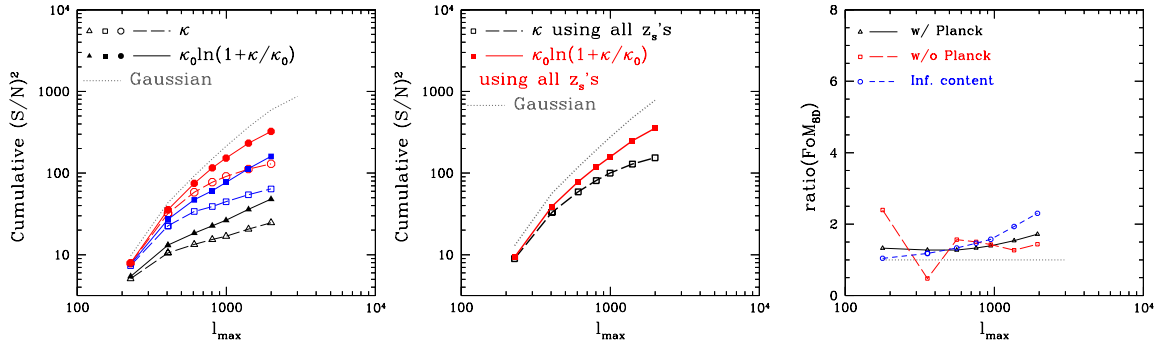

FIG. 7.— Left: the information content in the presence of shape noise ($\bar{n}_g = 30\,\mathrm{arcmin}^{-2}$ for each redshift bin). The dotted line shows the Gaussian limit in the presence of shape noise. Middle: the information content from the combination of the three source redshift bins. Right: the 8D FoM. We find very little improvement in the constraints on the final cosmological parameters once shape noise is added.

We can also quantify the improvement due to the log-transform using the Figure-of-Merit of dark energy parameters (hereafter '$\mathrm{FoM}_{w_0-w_a}$') that is often used in literature to characterize the performance of a dark energy survey mission. The Dark Energy Task Force (DETF) FoM (Albrecht et al. 2006) is defined as

$$\mathrm{FoM}_{w_0-w_a} \equiv \frac{1}{\sigma(w_p)\sigma(w_a)} = \frac{1}{\sqrt{\det(\mathrm{Cov}[w_0, w_a])}}, \quad (6)$$

where w_p is the dark energy equation of state at the "pivot" redshift, at which the dark energy equation of state is best constrained by given observables, and $\mathrm{Cov}[w_0, w_a]$ is the 2×2 sub-matrix of the inverted Fisher matrix, $\boldsymbol{F^{-1}}$, including only its elements of w_0 and w_a. The FoM is proportional to the area of the marginalized error ellipse in w_0 and w_a parameter sub-space. In Figure 6, the left panel shows $\mathrm{FoM}_{w_0-w_a}$ before (dashed lines) and after the log-transform (solid lines): we observe approximately a factor of two improvement when including the Planck prior (red and black lines with triangles).

In the middle panel, we show the 8-dimensional figure-of-merit as a function of $l_{\max}$. We find a factor of 7-12 improvement using $l_{\max} = 1000 - 2000$, which can be read out from the right panel where we show the ratio of FoM_{8D} between with and without the log-transform (black line). Table 2 presents the FoM values as a function of $l_{\max} = 1000 - 2000$.

TABLE 2
FIGURE OF MERIT.

$l_{\max}$	$\mathrm{FoM}_{w_0-w_a}$		FoM_{8D}	
	κ	$\kappa_{\ln}$	κ	$\kappa_{\ln}$
1000	301	803	3.56E+20	2.67E+21
2000	610	1423	1.90E+21	2.21E+22

NOTE. — Figure of Merit in w_0-w_a and in the 8-D before and after the log-transform.

5. FISHER MATRIX ANALYSIS WITH SHAPE NOISE

Any weak lensing survey contains shape noise, i.e., uncertainty associated with intrinsic shapes of the galaxies. This noise decreases with increasing galaxy number density. In the presence of large shape noise, the observed field is closer to Gaussian (assuming Gaussian shape noise) and $\kappa_{\min}$ is larger due to the additional dispersion: we therefore expect that a log-mapping will be less efficient for a larger shape noise. Paper I have shown that, with a galaxy number density of $30\,\mathrm{arcmin}^{-2}$ at $z_s = 1$ and a pixel size of 2.4 arcmin, a factor of the improvement is 2.4 for $l_{\max} = 2000$; we find a similar result of 2.3 as shown in the left panel of Figure 7. We assume the total mean number density of $90\,\mathrm{arcmin}^{-2}$ and the number densities of 30, 30, and $30\,\mathrm{arcmin}^{-2}$ for source redshifts of $z_s = 0.6$, 1.0, and 1.5, respectively. Note that this is a galaxy number density that is much higher than ground-
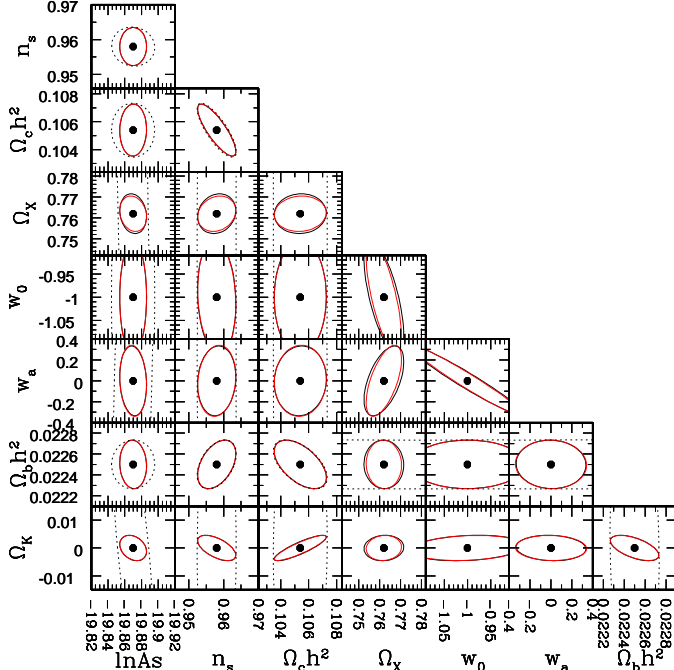
FIG. 8.— In the presence of shape noise ($\bar{n}_g = 30\text{arcmin}^{-2}$ for each redshift bin), we find little improvement in the constraints on the final cosmological parameters after log-transform. Black: before log-transform. Red: after log-transform.

based, near-future weak lensing surveys.

Figure 7 shows that, in the presence of this modest shape noise, the improvement in the information content due to the log-mapping is still large, but the 8D FoM is very similar for the standard κ estimator and for $\kappa_{\ln}$. The improvement on the full set of cosmological parameters is only a factor of 1.7 for $l_{max} = 2000$.

Figure 8 shows the marginalized error contours with the Planck prior in the presence of shape noise: the improvement due to the log-mapping is not found here despite the large degree of improvement in the information content. Therefore, we find the improvement in the information content by the log-mapping does not propagate efficiently to the improved cosmological information in the presence of even an optimistic limit of shape noise for future weak lensing surveys. The effect of shape noise we find is consistent with Joachimi et al. (2011) despite the different set of cosmological parameters investigated, except that they find much smaller improvement in the information content. In calculating the information content (Eq. 5), we set the signal to be an averaged power spectrum of the log-transformed field after subtracting a constant power as an approximation for the shape noise effect; Joachimi et al. (2011) use a power spectrum without shape noise as a signal. Since the constant power we subtract does not include higher order contributions that mingles shape noise and the clustering signal, the signal we input is higher than that of Joachimi et al. (2011) and therefore our information content is larger.

It is quite possible that the problem of the shape noise lies in the estimator. In the absence of shape noise, the log-transformed field is the obvious way to make the field nearly Gaussian. In the presence of shape noise, it is quite possible that one must work harder to find an estimator that recaptures the information lost to higher point functions. A different

Gaussianization scheme, particularly one not so sensitive to $\kappa_{\min}$, might well work better. It is also possible that the information is hopelessly lost due to the shape noise and there is not much to recover with log-transform. The encouraging results to date in the absence of shape noise suggest that this is an important avenue of research.

6. THE EFFECT OF THE PIXELIZATION

Using a larger pixel appears more efficient in terms of the information content than using a smaller pixel, whether with and without shape noise, partly due to the smaller $|\kappa_{\min}|$ that we can reach for a larger pixel. The top panels of Figure 9 shows the information content and the 8D FoM using a pixel of 0.6 arcmin, instead of our fiducial pixel of 2.4 arcmin, in the presence of no shape noise. From the left panel, one sees that the information content after log-mapping (left panels) is much lower when using a smaller pixel than when using a pixel of 2.4 arcmin (in Figure 1) (also see Neyrinck 2011b; Joachimi et al. 2011). On the other hand, we find that the difference in FoM_{8D} for different pixel sizes is not as drastic as we have expected based on the information content result. The left panel of Figure 10 shows the marginalized error contours for the pixel of 0.6 arcmin without shape noise and without the Planck prior. Since this case is less efficient for the log-transform, unlike the case of a 2.4 arcmin pixel (in Figure 4), the changes in the error ellipses are not a simple shrinkage of ellipses. The projections are that the $\kappa_{\ln}$ field leads to narrower allowed regions, which implies stronger degeneracies after the log-transform; the errors on cosmological parameters do not decrease after the log-transform despite the improvement in the information content. When the Planck priors are combined (right), the strong degeneracies in the power spectrum of $\kappa_{\ln}$ are lifted, and now the thin error ellipses observed in the left panel finally translate to smaller errors on Ω_X, w_0, and w_a.

The bottom panels of Figure 9 shows the information content and the 8D FoM using a pixel of 0.6 arcmin *in the presence of shape noise*. In comparison to Figure 7 for pixel of 2.4 arcmin, we find even less improvement with the log-transform due to a smaller pixel. The effect of pixel we observe appears consistent with the effect of smoothing in Joachimi et al. (2011).

7. ANALYTIC FISHER MATRIX RESULTS

We compare our *N*-body Fisher matrix results with the analytic Fisher matrix results using a Halofit (Smith et al. 2003) for the fiducial mapping. As shown in the left panel of Figure 3, the derivatives derived from the Halofit slightly deviates from the *N*-body results, especially on high l, such that those for the dark energy parameters appear similar to what was shown in Casarini et al. (2011). Due to the discrepancy in the nonlinear convergence power spectrum between the Halofit and the *N*-body result (Eifler 2011), there seems to be a bigger difference in the fractional derivatives (bottom left panel). We conduct a Gaussian Fisher matrix analysis using Halofit results and the Gaussian assumption: we call this 'Gaussian Fisher matrix results'.

We find the *N*-body Fisher result predicts better constraints on dark energy parameters than the Gaussian Fisher result, which is contrary to Casarini et al. (2011). In detail, the nonlinear covariance matrix increases the error bars, relative to the Gaussian case, which is expected; however, the *N*-body results appear to show less degeneracies between dark energy
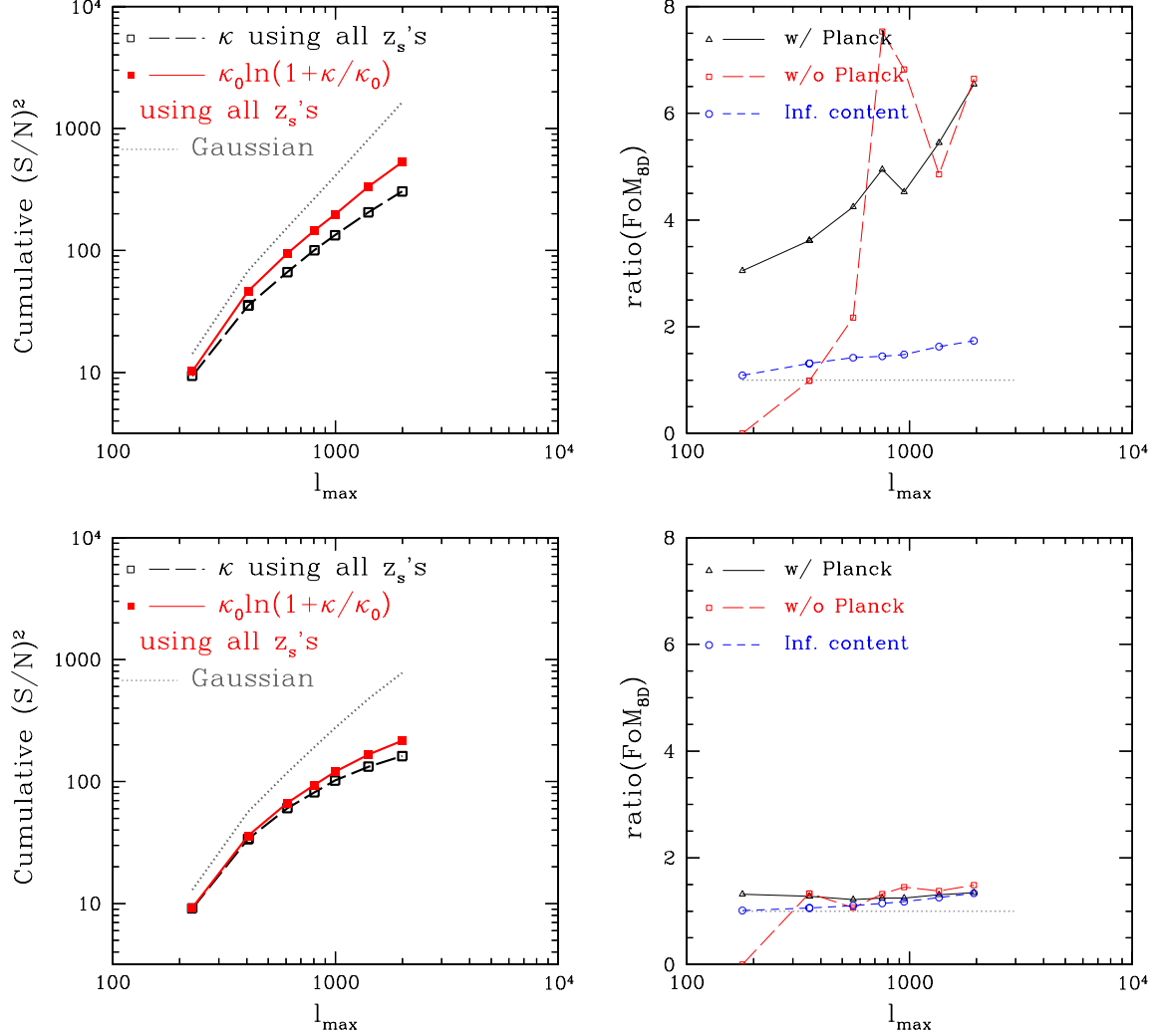
FIG. 9.— Effects of pixel size. We use a pixel of 0.6 arcmin for this figure. Top: without shape noise. Bottom: with shape noise ($\bar{n}_g = 30 \text{arcmin}^{-2}$ for each pixel). Left: the information content. Right: improvements due to log-mapping in terms of various quantities.

parameters (Ω_X, w_0, w_a) than predicted by Halofit. As a result, the N-body Fisher matrix analysis gives better constraints on dark energy parameters than the Halofit-based Gaussian case. If we hold w_a fixed or Ω_X fixed, the N-body FoM becomes worse than the Halofit result. In the presence of shape noise, the nonlinear covariance matrix is closer to the Gaussian one. Therefore the constraints from the N-body result are better than the Halofit-based Gaussian case to a larger extent. Table 3 lists our results.

We comment that sample variance introduces a noisy feature in the N-body derivatives. We have used $\Delta l = 200$ rather than a smaller bin width to reduce such noisy feature. However, any remaining noise might have affected the N-body results. We tried smoothing the derivatives, which did not decrease the constrains from the N-body results and therefore did not reverse our finding.

8. CONCLUSION

We have used the Fisher matrix formalism to test the impact of the log-transform on the cosmological parameters. We find that the log mapping performs much better than the fiducial

mapping: when Planck mission information is included as a prior, the log-transformed field greatly improves constraints especially on dark energy parameters such as Ω_X, w_0, and w_a. In the presence of shape noise, however, the advantage of the log mapping quickly diminishes. We find little improvement on the cosmological parameters after log-transform even with $\bar{n}_g = 30 \text{arcmin}^{-2}$ at each of the three source redshift bins. We find the information content is not necessarily a good probe of the actual precision on the final cosmological parameters. We also find using a larger pixel allows a more efficient log-transform with and without shape noise. Finally, we find that, for the fiducial mapping, the Halofit-based Gaussian Fisher matrix calculation gives worse constraints on dark energy parameters than the full N-body Fisher matrix result. This appears to be due to less degeneracies among dark energy parameters in the N-body power spectra.
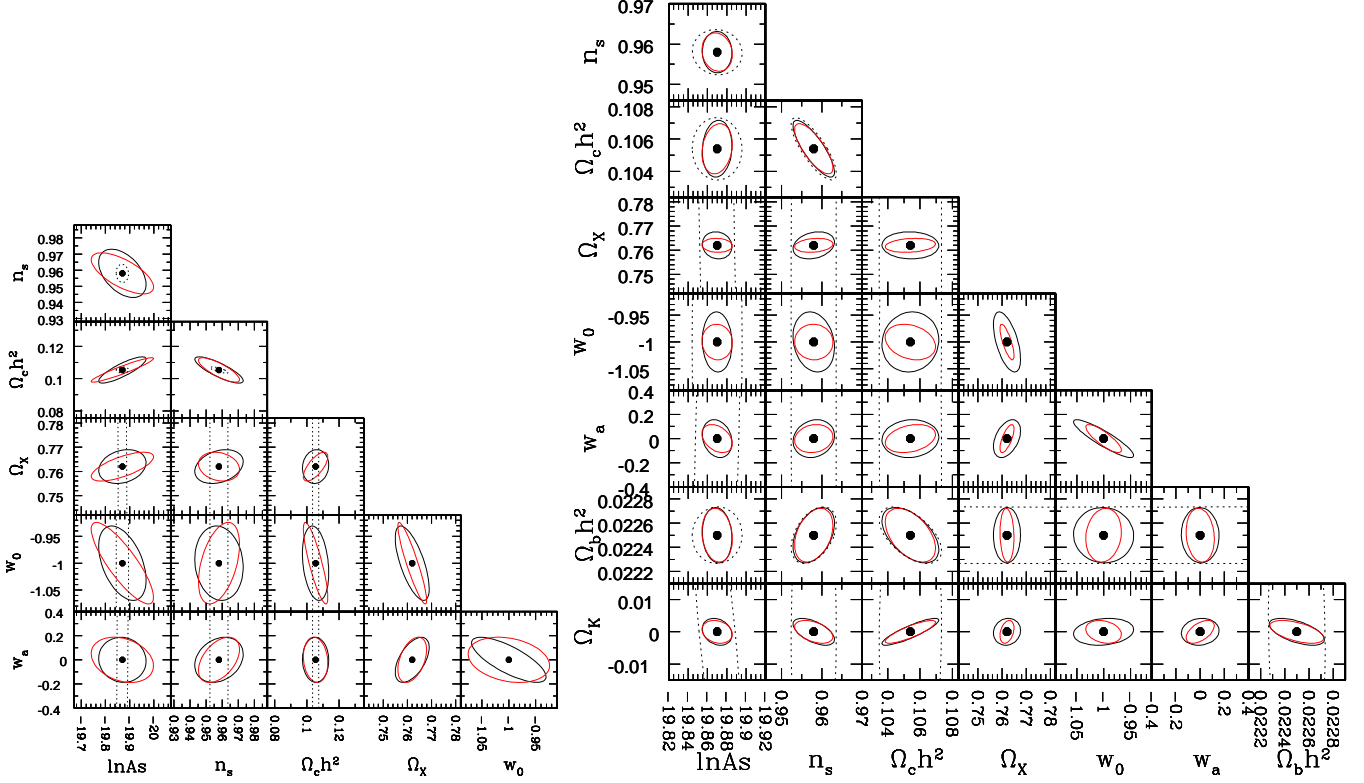
FIG. 10.— Effects of pixel size. Using a pixel of 0.6 arcmin. Marginalized error contours before (solid black lines) and after log-transform (red lines) without shape noise contamination. Left: without the Planck prior. Right: with the Planck prior. We use power spectrum information up to $l = 2000$. One sees that the log-transform is less efficient with a smaller pixel.

TABLE 3
N-BODY FISHER ANALYSIS VS ANALYTIC GAUSSIAN FISHER
ANALYSIS.

	Ω_X	w_0	w_a
κ + Planck	0.367E-02	0.357E-01	0.997E-01
Analytic	0.372E-02	0.451E-01	0.128
κ + Planck	0.335E-02	0.165E-01	–
Analytic	0.154E-02	0.154E-01	–
κ + Planck	–	0.294E-01	0.909E-01
Analytic	–	0.171E-01	0.530E-01
κ + Planck, shape noise	0.626E-02	0.808E-01	0.220
Analytic, shape noise	0.134E-01	0.169	0.409
κ + Planck, shape noise	0.525E-02	0.211E-01	–
Analytic, shape noise	0.429E-02	0.237E-01	–
κ + Planck, shape noise	–	0.603E-01	0.185
Analytic, shape noise	–	0.409E-01	0.131

NOTE. — The analytic Gaussian Fisher results are derived using the Halofit results and the Gaussian assumption. Shape noise is based on $\bar{n}_g = 30$ arcmin^{-2} for each source redshift bin. The results on parameters other than dark energy parameters are very similar between the two methods, mainly because these are dominated by the Planck information; we do not show these parameters in this table for simplicity. The rows with "–" means that the corresponding parameter is held fixed.

REFERENCES

T. Abbott *et al.* (Dark Energy Survey Collaboration), astro-ph/0510346.

Albrecht, A., et al. 2006, arXiv:astro-ph/0609591

Casarini, L., La Vacca, G., Amendola, L., Bonometto, S. A., & Macciò, A. V. 2011, JCAP, 3, 26

Coles, P., & Jones, B. 1991, MNRAS, 248, 1

Cooray, A., & Hu, W. 2001, ApJ, 554, 56

Eifler, T. 2011, MNRAS, 1490

Heitmann, K., White, M., Wagner, C., Habib, S., & Higdon, D. 2010, ApJ, 715, 104

Hikage, C., Takada, M., Hamana, T., & Spergel, D. 2011, MNRAS, 412, 65

Hu, W. 1999, ApJ, 522, L21

Hu, W. 2002, Phys. Rev. D, 65, 023003

Joachimi, B., Taylor, A. N., & Kiessling, A. 2011, arXiv:1104.1399

Kaiser, N. 1998, ApJ, 498, 26

Kayo, I., Taruya, A., & Suto, Y. 2001, ApJ, 561, 22

Meiksin, A., & White, M. 1999, MNRAS, 308, 1179

Neyrinck, M. C., Szapudi, I., & Szalay, A. S. 2009, ApJ, 698, L90

Neyrinck, M. C., Szapudi, I., & Szalay, A. S. 2011, ApJ, 731, 116

Neyrinck, M. C. 2011, ApJ, 736, 8

Neyrinck, M. C. 2011, arXiv:1105.2955

Sato, M., Hamana, T., Takahashi, R., Takada, M., Yoshida, N., Matsubara, T., & Sugiyama, N. 2009, ApJ, 701, 945

Sato, M., Takada, M., Hamana, T., & Matsubara, T. 2011, ApJ, 734, 76

Scoccimarro, R., Zaldarriaga, M., & Hui, L. 1999, ApJ, 527, 1

Seo, H.-J., Sato, M., Dodelson, S., Jain, B., & Takada, M. 2011, ApJ, 729, L11

Smith, R. E., Peacock, J. A., Jenkins, A., et al. 2003, MNRAS, 341, 1311

Takada, M., & Jain, B. 2004, MNRAS, 348, 897

Takada, M., & Jain, B. 2009, MNRAS, 395, 2065

Takahashi, R., et al. 2009, ApJ, 700, 479

Taruya, A., Takada, M., Hamana, T., Kayo, I., & Futamase, T. 2002, ApJ, 571, 638

Tegmark, M. 1997, Physical Review Letters, 79, 3806

Tegmark, M., Taylor, A. N., & Heavens, A. F. 1997, ApJ, 480, 22

Yang, X., Kratochvil, J. M., Wang, S., et al. 2011, Phys. Rev. D, 84, 043529

Yu, Y., Zhang, P., Lin, W., Cui, W., & Fry, J. N. 2011, Phys. Rev. D, 84, 023523